



# City Research Online

## City St George's, University of London

**Citation:** Sun, Z., Li, Q. & Bruecker, C. (2018). Short wavelength instability in the vortex ring during impingement onto a solid wall. Paper presented at the 19th International Symposium on Applications of Laser and Imaging Techniques to Fluid Mechanics, 16-19 Jul 2018, Lisbon, Portugal.

This is the accepted version of the paper.

This version of the publication may differ from the final published version. To cite this item please consult the publisher's version.

**Permanent repository link:** <https://openaccess.city.ac.uk/id/eprint/21650/>

**Copyright and Reuse:** Copyright and Moral Rights remain with the author(s) and/or copyright holders. Copies of full items can be used for personal research or study, educational, or not-for-profit purposes without prior permission or charge, unless otherwise indicated, provided that the authors, title and full bibliographic details are credited, a hyperlink and/or URL is given for the original metadata page and the content is not changed in any way. For full details of reuse please refer to [City Research Online policy](#).

# The Short-Wavelength Instability in the Impinging Vortex Ring Measured by Scanning-PIV

Zhengzhong Sun, Qianhui Li, Christoph Bruecker

Department of Mechanical Engineering and Aeronautics, City, University of London, UK

## 1. Background

The vortex ring is recently recognized as an efficient cooling methodology, thus giving rise to the unsteady fluid dynamic problem of impinging vortex ring. The head-on collision of vortex ring towards a surface is also widely adopted as a simplified model to understand the noise problem of an impinging jet. Considering its engineering background, thorough appreciation of the impingement process is essential for efficient engineering application.

### 1.1 Vortex ring impingement at a glance

Experiments on impinging vortex ring are not few. Earlier flow visualization [1] using colored dye revealed that the original ring expands in diameter when the wall is approached. In the meantime, a boundary layer is formed on the flat surface, which is subject to radial adverse pressure gradient. As soon as the boundary layer separates, it forms into a secondary ring in counter rotation, which subsequently orbits into the primary ring. The secondary ring is first subject to azimuthal instability, which manifests as the wave-like undulation along the ring torus. The appearance of azimuthal instability at the secondary ring triggers the interaction of the two vortex rings and leads to the loss of coherence and rapidly gives rise to turbulence. Note that, a tertiary ring can also be produced when the secondary ring moves into the primary one. The recent visualization experiment using laser induced fluorescent technique in the axisymmetric plane by New et al. [2] confirmed the previous observations. The authors reported the impingement process in the wall-parallel planes through the Scanning-PIV technique [3], which offers a perspective not available before. In this experiment, the azimuthal instability was measured quantitatively, and its evolution was revealed through auto-correlation method.

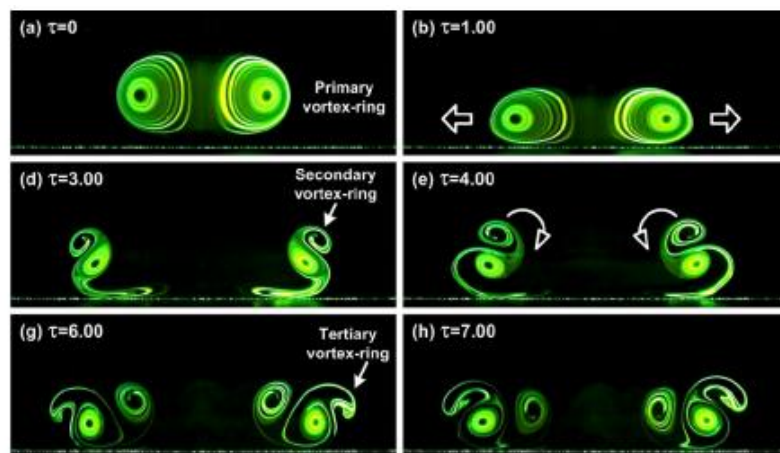


Figure 1. The impingement process visualized through laser induced fluorescent. [2]

## 1.2 The short wave-length instability

Apart from experimental works, a DNS study [4] made further advance about this flow problem and reported a short-wavelength instability (SWI) that develops on the impinging vortex ring, which was not noticed before. Different from the viscous wall condition in the experiment, this DNS simulation artificially applied the symmetric boundary condition at the impingement plane. Viscosity on the wall is hence neglected and no boundary layer is formed, nor is the generation of secondary ring. A question is naturally raised: is the SWI still present in reality where viscous wall is present? This question thus motivates the present experimental study using Scanning-PIV.

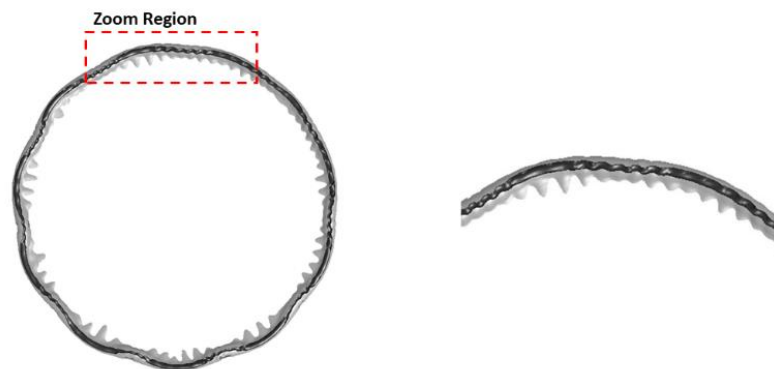


Figure 2. The short-wavelength instability visualized through DNS (left) and its lose-up view (right) [4].

## 2. Experimental Setup

The experiment is carried out in a water tank with dimensions of 300 (W) x 300 (L) x 400 (H) mm<sup>3</sup>. The vortex ring is produced through a piston-nozzle mechanism. The nozzle has outlet diameter of 30 mm. The piston is driven by a LinMot linear motor. In the experiment, the piston stroke is set to 85 mm, resulting in a formation number of 2.83. The piston velocity is 58.5 mm/s and the resulted vortex ring has a velocity of 40.6 mm/s. The piston based Reynolds number is 1,755 and the circulation based Reynolds number is 1,800. A square transparent glass plate with size of 150 (W)x150 (L) is place 130 mm below the nozzle outlet for impingement.

The impingement process is measured by Scanning-PIV. The flow illumination is provided through a 5W continuous wave laser with beam diameter of approximately 3mm. The laser sheets are formed through a drum scanner, which contains 20 mirrors evenly distributed along the drum's circumference. In the present experiment, the mirror arrangement generates 10 parallel slices with 1 mm vertical displacement and each slice is scanned twice in one evolution. The entire scan volume covers a vertical depth of 10 mm. The scanner is driven by a DC server motor at 3750 rpm, thus each plane is scanned at a rate of 125 Hz. The polymer particles are used as flow tracer. The particle density is close to that of water with nominal diameter of 40 $\mu$ m. A Phantom Miro310 high-speed camera is used to record the particle images. Since the camera is mounted at the side of the tank, a 45° first surface mirror is used to reflect the illuminated flow slice. This camera is equipped with a telecentric lens to ensure the same spatial resolution along the vertical depth. The camera is synchronized with

the scanner and the exposure time is set  $780 \mu\text{s}$  to match the time used in slice formation. A sketch of the flow facility and the measurement system is shown in figure 3.

Each measurement generates a data ensemble of 8000 images, they are later grouped into 10 slices to carry out sequential cross-correlation. The time separation between two images in the same slice is  $1/125 \text{ s}$ , which ensures time-resolved measurement. Apart from the Scanning-PIV measurement, a typical planar PIV measurement is carried out in the vertical plane which passes through the vortex ring axis. This planar PIV measurement records the impingement through a conventional point of view, which has been adopted by most of the previous works.

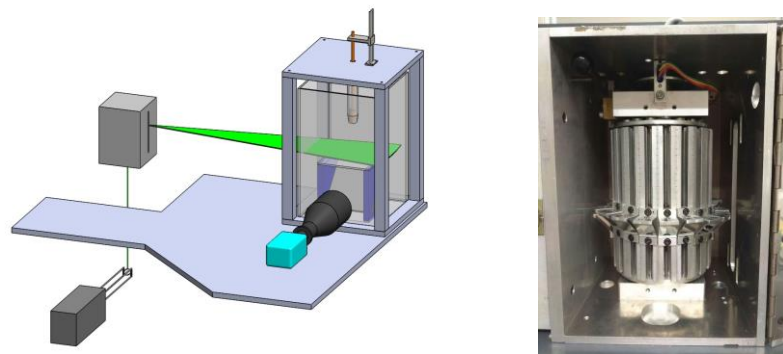


Figure 3. Experimental setup: (left) the conceptual sketch; (right) the drum scanner and mirror arrangement.

### 3 Results

#### 3.1 An overview of the impingement

The present impingement is found to follow the typical process as visualized before. Synthetic particle images are generated by adding 10 images together, so that the particle trajectories can be visualized. One snapshot of the synthetic image is shown in figure 4, where the primary and secondary vortex rings are both visualized through the swirling particles. This snapshot corresponds to the moment when the secondary ring moves on top of the primary one. In this figure, the top scanning laser slice is also indicated, which passes through the median plane of the primary ring. The rest of the scanning laser slice moves progressively to the lower positions with the downward step of  $1\text{mm}$ .

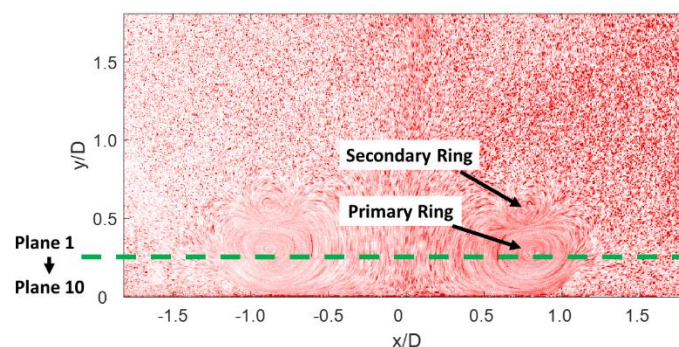


Figure 4. A synthetic particle image showing the primary and secondary vortex rings. The position of the top scanning plane (Plane 1) is also indicated.

In order to reveal the impingement process, the radial velocity  $U_r$  along the entire radius at phase angle  $\theta=0^\circ$  is extracted from the data ensemble and plotted along the temporal axis. The results in Plane 9 is shown in figure 5. It is rather clear that the primary vortex ring expands from the snapshot  $N=1200$  to  $N=2100$ , which is determined through the outward motion of the peak  $U_r$ . Together with the expansion of the primary ring, the secondary ring is produced at around  $N=2000$ , when negative  $U_r$  appears beyond positive  $U_r$ . Tertiary ring is produced at around  $N=3000$ , as revealed through the simultaneous appearance of the positive and negative  $U_r$ . It is also conjectured that a fourth ring also tends to form at  $N=4000$ . From  $N=4500$ , the positive  $U_r$  has intermittent appearance and the consistent appearance of  $U_r$  is finally terminated at around  $N=5200$ , which suggests the interaction of the primary and secondary rings.

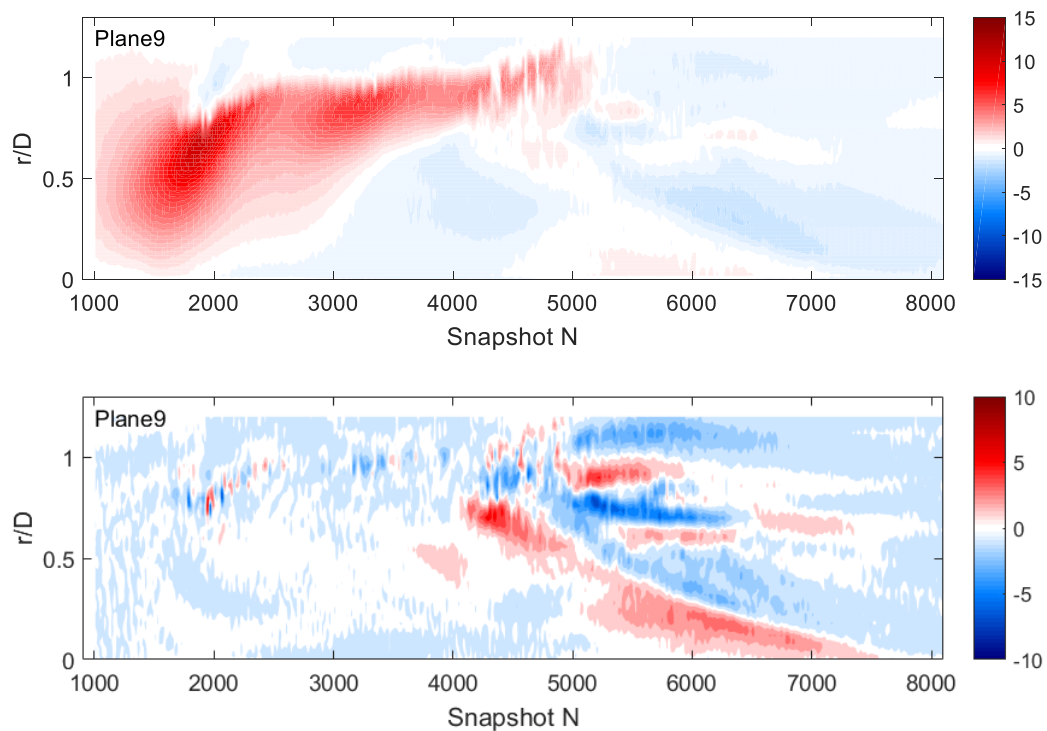


Figure 5. Temporal evolution of the radial velocity  $U_r$  [cm/s] (a) and axial vorticity  $\omega_z$  [1/s] (b) along the radius at  $\theta=0^\circ$  in Plane 9 (the bottom plane).

The interaction process can be better represented through the axial vorticity  $\omega_z$ . The alternating axial vorticity magnitudes begin to show up at  $N=4200$ , suggesting the initiation of the azimuthal instability. Since the axial vorticity and intermittency of the radial velocity appear simultaneously, they are closely linked. It can be conjectured that the latter is caused by the former. The alternating strips of positive and negative vorticity persist from  $N=4200$  to  $N=7000$ , which suggests the duration of the interaction process. After  $N=7000$ , the coherence of vorticity is completely lost and turbulence is generated.

So far, there is still the question: when does the short-wavelength instability (**SWI**) takes place. If close attention is paid to the interface between the positive and negative radial velocity in figure 5(a), the interface is not smooth and indicates undulation at high frequencies. At the same location of the velocity interface, axial vorticity of small scale is generated. In order to

understand this small-scale activity, the horizontal plane is investigated in the following subsection.

### 3.2 Visualization of the Short-Wavelength Instability

The snapshot at  $N=1968$  is chosen to reveal the high-frequency undulation observed in the previous section. The contours of radial velocity and axial vorticity within the bottom plane (Plane 9) are shown in figure 6. This snapshot corresponds to the moment when the secondary ring is being formed. In the contour of radial velocity, the primary ring is indicated by the circular positive radial velocity, while the secondary ring is represented by the negative magnitude. The weaker magnitude of the secondary can be found through the much smaller negative velocity magnitude, namely about  $-2$  cm/s. The non-smooth interface between the two rings is also visualized, and the interface corrugation is more pronounced on the right-hand side. The interface undulation gives rise to axial vorticity as shown in contour of axial vorticity. In association with deeper interface undulation, stronger axial vorticity magnitude is produced on the right. It is now apparent that the small-scale axial vorticity is aligned with the circular interface. More importantly, the positive and negative axial vorticity appear in an alternating pattern, conforming with vorticity pattern caused by an azimuthal instability. As the top and bottom portions of the circular interface are cropped by the camera field of view, accurate identification of the wavenumber is not possible. But it is certain that the wavenumber of the interface instability is of much shorter wavelength than the wavenumber in the secondary ring and that exhibited in the transition of this ring, which is around 7. The present SWI is different from that in the DNS study [4], as the SWI in the latter appears simultaneously with the long-wavelength instability. So far it can be concluded that the SWI appears when the secondary ring is being produced and it is at the interface between the primary and secondary ring.

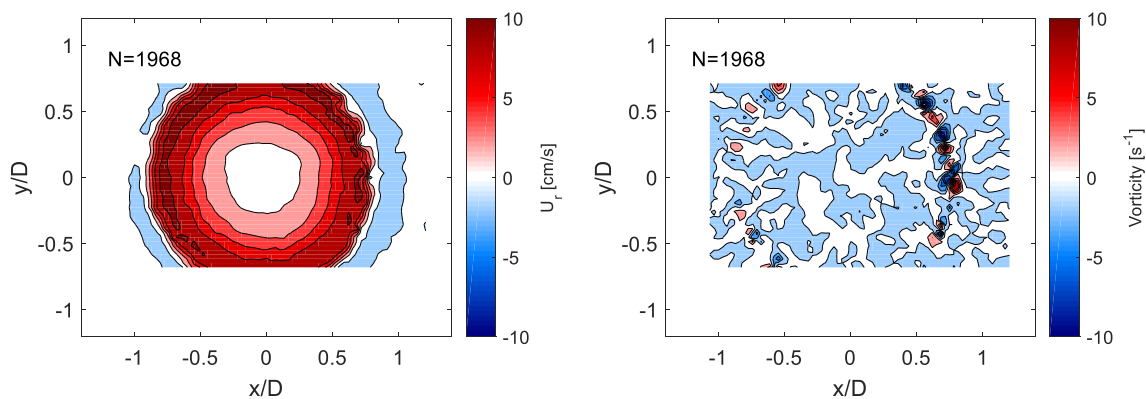


Figure 6. Contour of radial velocity (left) and axial vorticity (right) at  $N=1888$  in Plane 9.

## 4 Conclusions

The Scanning-PIV has been successfully implemented into the vortex ring impingement onto a solid surface. The present impingement process conforms with the other vortex ring impingement in general, including primary expansion, secondary generation, interaction of the vortex rings and turbulence production. The temporal evolutions of the radial velocity and axial vorticity have been studied. The interaction between primary and secondary ring

manifests in the coherent generation of axial vortical and the intermittent positive radial velocity. Following the progress of interaction, the coherence of primary ring is completely lost. Special attention is paid to the SWI revealed by other researchers. The SWI is found to appear at the interface between the primary and secondary rings, and makes the interface corrugated. The present SWI does appear earlier than the vortex ring interaction, hence it is independent from the long-wavelength azimuthal instability wave behaved by the secondary ring.

## References

- [1] JDA Walker, CR Smith, AW Cerra, TL Doligalski, The impact of a vortex ring on a wall, *J. Fluid Mech.*, 181:99-140, 1987.
- [2] TH New, S Shi, B Zhang, Some observations on vortex-ring collision upon inclined surface, *Exp. Fluids*, 57:109, 2016.
- [3] Z Sun, Q Li, C Bruecker, Vortex ring impingement measured by Scanning-PIV, 12<sup>th</sup> International Symposium on Particle Image Velocimetry, June 18-22, 2017, Busan, Korea.
- [4] PJ Archer, TG Thomas, GN Coleman, The instability of a vortex ring impinging on a free surface, *J. Fluid Mech.*, 642:79-94, 2010.